Science and Innovation of Advanced Materials

The Materials Research Society of Thailand

Research Article

Soft X-ray Spectroscopy on Titanium-based Decorative Coatings Prepared by Cathodic Arc Deposition

Hideki Nakajima[1,*], Wuttichai Phae-ngam[2], Viboon Taoanwong[3], Tossaporn Lertvanithphol[4], Mati Horprathum[4]

[1] Synchrotron Light Research Institute, Muang, Nakhon Ratchasima 30000, Thailand
[2] Physics program, Phranakhon Rajabhat University, Bangkhen, Bangkok 10220, Thailand
[3] Thapanin Co., Ltd., Bangpleeyai, Bangplee, Samutprakarn 10540, Thailand
[4] Opto-Electrochemical Sensing Research Team, Spectroscopic and Sensing Devices Research Group, National Electronics and Computer Technology Center, Pathum Thani 12120, Thailand

* Corresponding author e-mail: hideki@slri.or.th

Received: *June 15th, 2022* | ***Revised:*** *August 30th, 2022* | ***Accepted:*** *August 30th, 2022*

Abstract: The electronic structure of titanium-based decorative films such as titanium oxides, nitrides, carbides, and their mixtures was measured by soft X-ray photoemission and absorption spectroscopies. The titanium-based decorative films were deposited on a silicon wafer by the cathodic arc method with various gases at different flow rates resulting in diverse colors for decorative coatings to be applied to metal surfaces. However, it is difficult to control and characterize the coloration of titanium-based decorative films under various methods and conditions. In this study, the colorful titanium-based decorative films are analyzed in terms of elemental and chemical compositions to provide a fundamental principle of coloration for decorative coatings.

Keywords: Titanium based coating, Soft X-ray spectroscopy, Cathodic arc deposition, Coloration

1. Introduction

Titanium (Ti) based decorative film such as titanium nitride (TiN) is a typical hard coating that needs wear and corrosion resistance on metal and plastic surfaces. Ti-N bonds based on a combination of covalent, metallic, and ionic bonds result in ceramic-like hardness and chemical inertness as well as electrical and thermal conductivities [1]. TiN is also gold-like and biocompatible, so the coating is decorative and functional in medical tools and implants [2,3]. The gold color in TiN films is attractive, especially for watchmakers to decorate specific parts with high functionality, such as wear and corrosion resistance, without using the gold coating. These excellent properties of TiN coatings are like the diamond-like carbon (DLC) coating [4,5]. A type of DLC called tetrahedral amorphous carbon (*ta*-C) for hard coating provides a higher hardness and lower friction than TiN [6]. However, due to its hardness, *ta*-C has high internal stress that causes discontinuity at the interface resulting in poor adhesion to the substrate [7,8]. In addition, the color of *ta*-C ranges from anthracite to black. The color of DLC varies on the hydrogen contents, drastically changing the hardness of DLC [9,10]. The color of TiN films varies from gold to black upon the elemental and chemical compositions that provide various applications with and without degrading tribology [7]. A drawback of TiN coating is

the temperature range limited to below 600 °C due to the surface oxidation, which modifies the color and wear resistance [11].

The coloration in films is primarily attributed to the electronic structure in a way that visible light is absorbed and emitted between the valence and conduction bands resulting in a specific color for human eyes [7,11]. Second, an interference between substrate and film enhances and suppresses a particular wavelength from its color spectrum [12,13]. Third, the morphology and porosity of films play an additional role in the coloration of films via scattering and diffusion. A major challenge of coating is to produce a designed color with high wear and corrosion resistance. However, the color of Ti-based films from the point of view of the electronic structure has not been investigated yet because its application is highly valuable to decorations such as shiny jewelry.

From the point of the electronic structure, TiN is a promising candidate for *p*-type metal gate electrodes for high-κ metal-oxide-semiconductors (MOS) to replace poly-Si/SiO_2 MOS because of a tunable and effective work function of TiN interface with HfO_2 and $LaLuO_3$ to reduce the energy of consumption and thickness of devices [14-17]. TiN also shows plasmonic properties upon its crystallographic, microscopic structures, and surface oxidation [18-20].

This work analyzes the electronic structures on the Ti-based decorative films fabricated by cathodic arc deposition (CAD), widely used for large-scale and complex 3D coating in the industry without filters. CAD produces evaporation and ionization simultaneously so that the target compositions directly transfer to the substrate at a high deposition rate. The color, texture, and stress of films depend on various conditions in a deposition process. In particular, the reactive gases and their flow rates play a vital role in the coloration of films based on the elemental and chemical compositions [11,21]. It should also be noted that the TiN films are prone to oxide on the surface immediately after air exposure and thermal treatment [22,23]. The scope of this work not only discloses the surface chemistry of decorative and practical Ti-based coatings but also analyzes the relation of chemical compositions between the surface and bulk of films in combination with soft X-ray photoemission spectroscopy (XPS) and soft X-ray absorption spectroscopy (XAS).

2. Experimental

The color of the Ti-based decorative films was evaluated by ColorQuest XE spectrophotometer (HunterLab) in the Commission Internationale de l'éclairage (1931) CIELAB (1976) standard colorimetric space based on the brightness (L^*), and chromaticity (a^* and b^*) under CIE standard illuminant D65 [24].

The Ti-based decorative films (1 TiO_2 and 5 TiN-based samples) were prepared by an industrial cathodic arc deposition system (HCCA-2228, Guangdong Huicheng Vacuum Technology Co., Ltd., China) installed at Thapanin Co., Ltd (Thailand) as illustrated in Figure 1. The cathode material is Ti at 99.99% purity. The high purity gases (99.99%) of argon (Ar), oxygen (O_2), nitrogen (N_2), and acetylene (C_2H_2) were used to control the color of films so that Ti-based films can be titanium carbide (TiC), nitride, oxide, and their combinations including titanium carbonitride (TiCN) and oxynitride (TiON). However, detailed parameters and conditions are not disclosed because the color of the films deposited is not reproducible or stable in each coating process. The deposition chamber was evacuated to a base and operating pressure below 10^{-5} and 10^{-1} Pa, respectively. A mirror-polished silicon wafer was used as a substrate. The substrates were ultrasonically cleaned in acetone and ethanol prior to the deposition. A mass-flow controller controls the flow rate. The arc potential applied to the cathode is 300 volts. The substrate is biased at 100 volts, and its temperature is 100-150 °C. The sample stage in the carousel was rotated at a speed of 20 rpm to make a film homogeneous. The film thickness is varied in the range of 50-470 nm measured in field emission scanning electron microscopy (FE-SEM).

Ultraviolet photoemission spectroscopy (UPS), XPS, and near-edge X-ray absorption spectroscopy (NEXAFS) measurements were performed at BL3.2Ua in Synchrotron Light Research Institute (SLRI, Thailand) [25,26]. UPS and XPS spectra were measured by the CLAM2 electron energy analyzer (Thermo VG Scientific) at the emission angle of 20°, and the incident angle of light is 70°. The light polarization is parallel to the sample surface. Light intensity was monitored at the gold mesh in front of the sample to normalize the spectra. The sample surface is grounded by carbon

tapes and kept at room temperature. Synchrotron radiation from the planar undulator (U60) is used to excite the photoelectron from the sample surface. The U60 gap is fixed at 26.5 mm. No etching was performed prior to the measurements to prevent the artifacts from sputtering damage [27,28]. The information depth of UPS and XPS is about 3 nm from the surface [29,30].

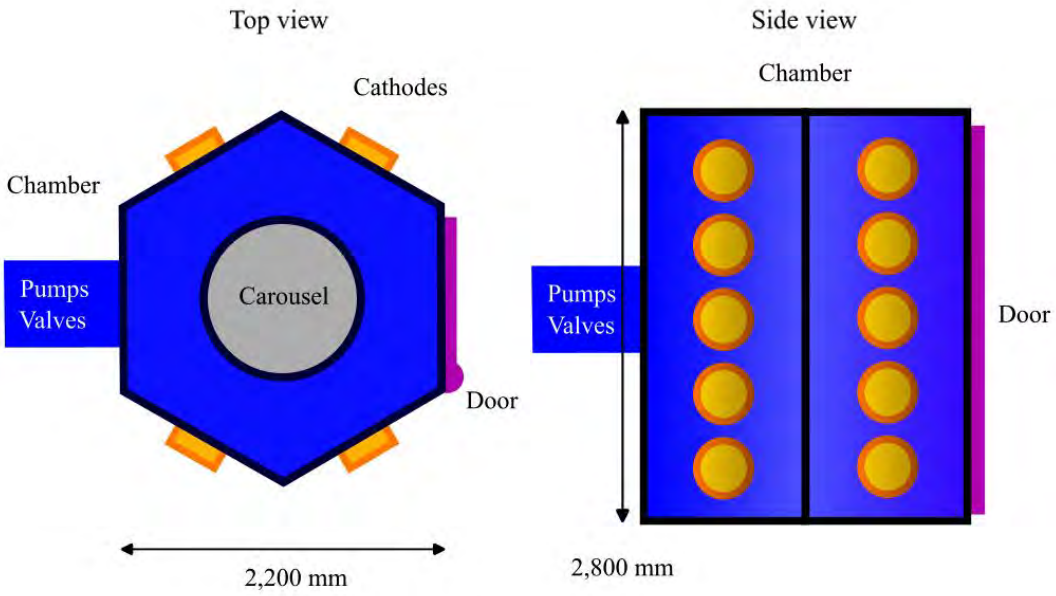

Figure 1 A schematic drawing of the cathodic arc deposition setup from the top (left) and side (right) views.

The UPS spectra were measured at the photon energy of 39.5 eV, and samples were negatively biased to extract the low kinetic energy electrons (secondary electrons). The binding energy of UPS spectra is referenced from the Fermi edge of gold. The work function is calculated from the cutoff energy, and the total energy resolution of UPS is 0.15 eV at the pass energy of 10 eV in the energy analyzer.

The XPS spectra were measured at the photon energy of 600 eV. The total energy resolution is about 2 eV at the pass energy of the energy analyzer is 50 eV. The binding energy of XPS spectra is referenced from the work function method described elsewhere [28,31-33].

The NEXAFS spectra were measured at the C, O, N *K*, and Ti $L_{3,2}$ edges in the total electron yield (TEY) and fluorescence yield (TFY) modes at the same sample position as XPS. TEY is measured from the sample drain current, and TFY is measured at the multichannel plate photocurrent. All the NEXAFS spectra were normalized by the photon flux monitored from a drain current of a gold mesh in front of the sample. However, because the gold mesh is also contaminated by carbon, the photon flux decreases at the C *K* edge. To remove the effect of carbon contamination at the gold mesh, all the C *K* edge spectra were further normalized by the C *K* edge spectrum of clean gold which is supposed to be the incoming flux at the sample [34,35]. The photon energy of NEXAFS spectra is referenced from the C1s to π* transition at 285.38 eV on highly oriented pyrolytic graphite [36].

All the spectra were analyzed in the XPS analysis macro suite (EX3ms, version 8.47) on Windows Microsoft 365 Excel (version 2204) from the calibration to peak fitting procedures [37].

3. Results and discussion

Figure 2 shows the color of samples characterized in this report. The color of samples is evaluated in the CIE 1976 color space as listed in Table 1. The horizontal and vertical axes represent the chromatic parameters *a** and *b**,

and the radius of markers the lightness (L^*). The CIE parameters of the Brass color are quite like those of white gold. However, the colors are well characterized by the CIE parameters such as a^*, b^*, and L^*. The picture of samples is presented in the inset of Figure 2. It is found that L^* decreases as b^* decreases, which is against the previously reported results [11].

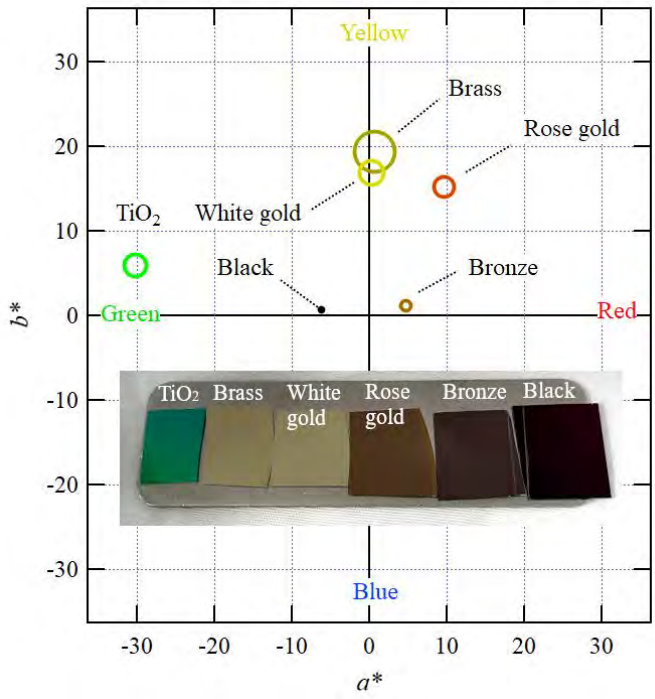

Figure 2 Color plot based on CIE standard reference. Brightness (L^*) is represented by the radius of circle markers. The inset of the figure shows the sample colors and names used in the characterization.

Table 1 The valence band maximum (VBM), cutoff energy, work function (WF), C1s C-C peak reference energy, thickness, and CIE parameters are listed for each sample. The atomic concentrations of each element evaluated in XPS are also listed.

Name	TiO_2	Brass	White gold	Rose gold	Bronze	Black
Cutoff, eV	35.38	35.03	34.84	35.02	35.04	34.81
WF, eV	4.12	4.47	4.66	4.48	4.46	4.69
C1s (C-C), eV	285.46	285.11	284.92	285.10	285.12	284.89
VBM, eV	3.68	3.00	2.90	3.18	3.18	3.22
Thickness, nm	n/a	43	68	49	237	469
L^*	60.14	79.40	62.18	57.18	46.65	38.75
a^*	-30.30	0.63	0.28	9.62	4.73	-6.29
b^*	5.90	19.39	16.90	15.25	1.22	0.73
C, at. %	36.1	32.9	27.5	40.7	46.3	51.2
O, at. %	46.3	39.1	41.4	38.9	36.1	36.5
N, at. %	1.6	11.6	11.5	7.4	7.8	3.4
Ti, at. %	16.0	16.4	19.6	13.0	9.8	8.9

Figure 3 shows the UPS spectra on the sample surface. UPS spectra in Figure 3 are normalized at the intensity and subtracted by the constant background. Figure 3(a) plots the secondary electron cutoff to evaluate the work function (WF) as shown in Table 1. The work function of TiN-based coatings varies between 4.46 and 4.69 eV, which agrees with the literature [14]. WF depends on the morphology at the surface and chemical potential in bulk [38,39]. The sharp slope of the cutoff represents the homogeneous surface in morphology, which suggests that WF varies upon the chemical potential rather than the electrostatic potential cut [40]. Figure 3(b) shows the valence band maximum (VBM). The Fermi edge of gold is clearly identified at the zero of binding energy. VBM is deep on TiO_2 (3.68 eV), and VBM of TiN-based films shifts toward low binding energy on Brass (3.0 eV) and White gold (2.9 eV), and then the other samples (3.18-3.22 eV). The morphology and optical properties measured by X-ray diffraction, electron microscopy, Raman spectroscopy, and ellipsometry will be reported elsewhere.

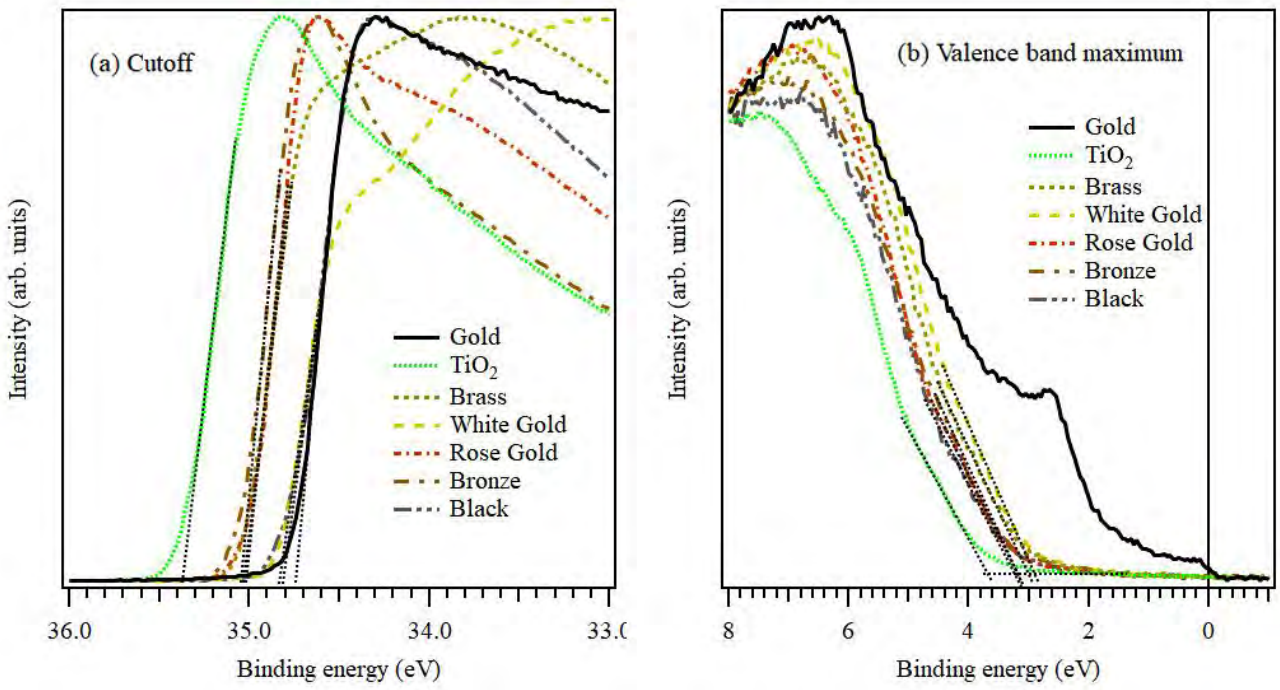

Figure 3 UPS spectra on (a) secondary electron cutoff and (b) valence band maximum measured at the photon energy of 60 eV.

Figure 4 shows the XPS spectra for the survey scan and the elemental compositions of each sample evaluated from the spectral fitting presented in Figure 5. C1s, O1s, N1s, and Ti2p3/2 peaks are used to evaluate the atomic concentration based on the peak fitting procedures [41]. In Figure 4(a), each peak is discerned from the Auger peaks and secondary electron background, which increases at the low kinetic energy. The atomic concentrations of the elements on the surface of the TiO_2 and TiN-based films in Figure 4(b) and Table 1 were evaluated from each peak area normalized with the relative sensitivity factor corrected by the photoionization cross-section at 600 eV [42,43]. Carbon contamination and surface oxidation cannot be avoided during the deposition and sample transfer to the analysis system, so carbon and oxygen are dominated in the compositions. However, nitrogen and titanium are still visible to identify the surface chemical compositions to be discussed in Figure 5. The non-stoichiometric content in Ti and O in TiO_2 is based on surface oxidation and termination. A trace of nitrogen in TiO_2 is also found at 1.6%, which might be due to the low vacuum operation or leakage in the gas flow system. The nitrogen content is high in Brass

and White gold, medium in Rose gold and Bronze, and low in Black samples. The carbon content is high in Rose gold, Bronze, and Black samples upon the hydrocarbon gas flow rate.

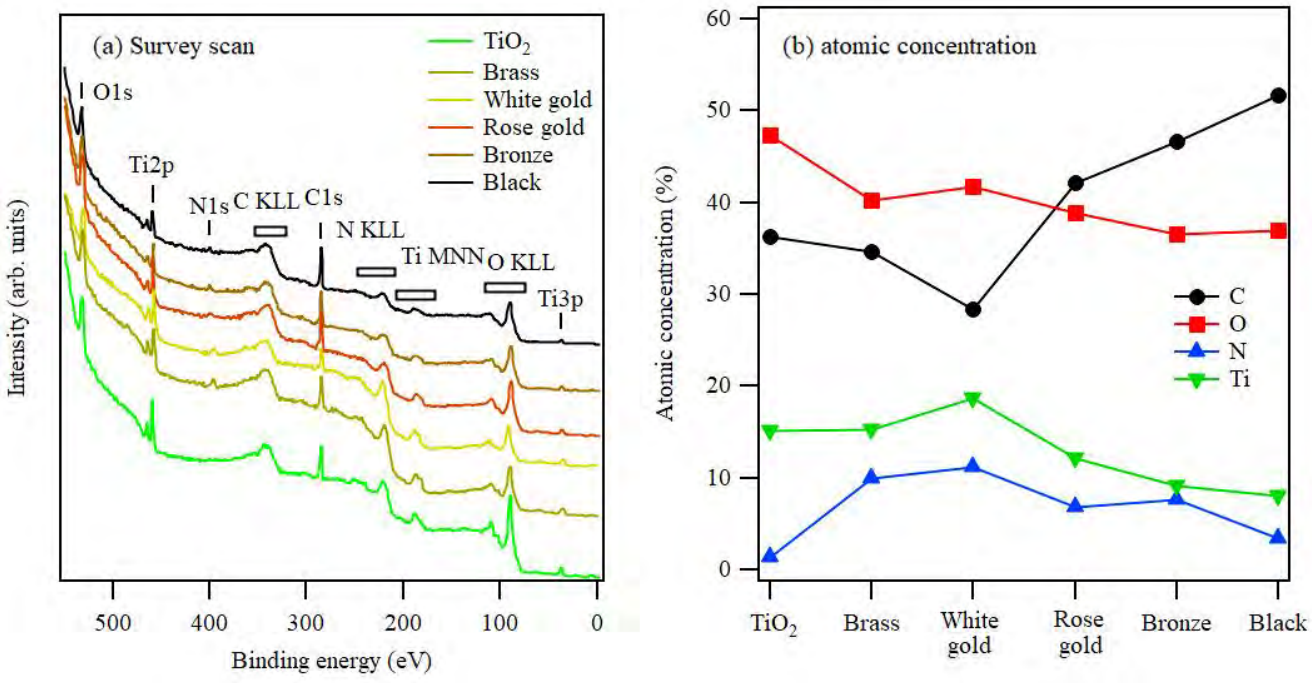

Figure 4 XPS survey and elemental compositions. (a) XPS survey scan spectrum measured at the photon energy of 600 eV, and (b) elemental compositions evaluated from the spectral fitting to be presented in Figure 5.

Figure 5 represents the fitting results of XPS spectra for elemental and chemical compositions. All peaks are fitted with a Gaussian shape at the full-width half maximum (FWHM) of 2 eV, except for Ti2p. Ti2p spectra were fitted with a pseudo-Voigt function described by a weighted sum of a Gaussian and Lorentzian function. Their FWHMs are in the range between 1 and 3 eV. FWHM of Ti2p1/2 is typically broader than that of Ti2p3/2 because Ti2p1/2 has the Coster-Kronig process. The relative weight of the Gaussian is 80%, and the rest is from the Lorentzian contribution.

Figures 4(a-d) show each synthetic peak and background line indicated by the black dash and solid lines, respectively. The sum of synthetic peaks and background lines is presented in the solid red line over the raw spectra presented by the open circle markers. The backgrounds of C1s and Ti2p spectra are analyzed by Shirley's type, and the other two spectra are based on the spline curves. O1s spectra appear on the high secondary electron background, which is simulated by the spline shape. N1s spectral intensity is too small to apply Shirley's type background, so the spline background was used because the secondary electron is dominant in its background. All the background subtraction is simultaneously optimized with the peak fitting procedure, which is the so-called active approach [41].

C1s spectra in Figure 5(a) were fitted with 3 peaks as indicated by C-(1-3), O1s spectra in Figure 5(b) with 3 peaks as indicated by O-(1-3), and N1s spectra in Figure 5(c) with 6 peaks as indicated by N-(1-5). Ti2p spectra have a doublet structure in a way that Ti2p3/2 and 1/2 peaks appear in the energy difference defined by the spin-orbit splitting at 5.9 eV and their amplitude ratio is 2:1 based on the multiplicity of the total angular momentum, j =3/2 and 1/2. As shown in Figure 5(d), Ti2p3/2 can be fitted with 4 peaks as indicated by T-(1-4), and their analogous peaks appear in Ti2p1/2 as well.

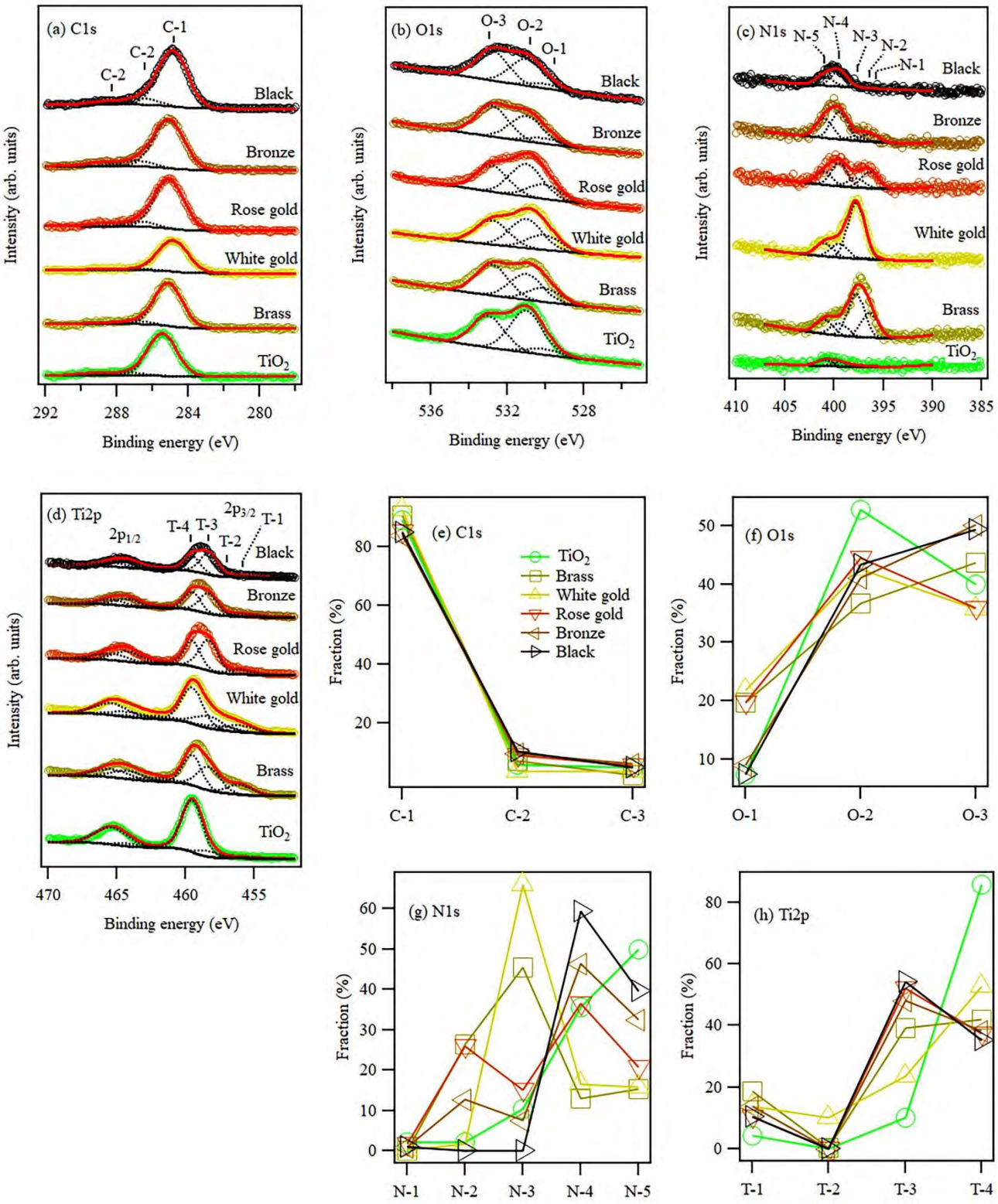

Figure 5 XPS spectra fitted with background and multiple peaks on (a) C1s, (b) O1s, (c) N1s, and (d) Ti2p. Chemical compositions are also plotted for (e) C1s, (f) O1s, (g) N1s, and (h) Ti2p.

According to the previously reported paper [44], the chemical states are assigned in a way that C1s peak is composed of C-C/C-H (C-1), C-O (C-2), and O=C-O (C-3) [45]. The O1s peak has TiO-1), C-O/O=C-O, TiO_xN_y (O-2), and H_2O/N-O or weakly adsorbed oxygen (O-3) [46], and N1s has TiO_xN_y (N-1, N-2), TiN (N-3), TiN-sat/pyridinic-N (N-4), and pyrrolic-N/N_2 (N-5) [44,47]. The pyridinic-N and pyrrolic-N originate from a nitrogen atom in the π-conjugated carbon network, and N_2 is molecular nitrogen. Ti2p has TiN (T-1), TiO_xN_y (T-2), TiO-III/TiN-sat (T-3), and TiO-IV (T-4) [44,48,49]. TiO-III includes titanium oxides involved with C and N atoms. All the fitting parameters are listed in Table 2.

The chemical compositions of C1s in Figure 5(e) are primarily based on C-C/C-H bonds even though the hydrocarbon is fed into the deposition process. C-O and C=O bonds are minor and slightly varied among the samples. The chemical compositions of O1s in Figure 5(f) are moderately changed among the samples. However, the TiO_2 bond is less contributed than the others, even in the TiO_2 sample. These results indicate that the sample surface is modified by carbon contamination and oxidation. Therefore, it is difficult to distinguish the chemical compositions of films from the surface chemical compositions of carbon and oxygen. It is also found that the TiO_2 fraction is high in Brass, white, and rose gold samples, which might have more surface oxidation than the others.

The chemical compositions of N1s in Figure 5(g) suggest a relation between the color and nitrogen bond. A noticeable trend is seen in Figure 5(c), which shows the N1s peaks are distributed toward the high binding energy from the second bottom (Brass) to the top of spectra (Black), and the distribution of peaks is sparser and less intense. Brass and White gold are firmly based on the TiN bond. Rose gold splits the TiN peak into TiO_xN_y and pyridinic-N/TiN-sat without a distinct TiN peak. Bronze and Black highly depend on pyridinic-N/TiN-sat and pyrrolic-N/N_2 bonds [50]. Note that TiN-sat should follow the ratio of the TiN peak because TiN-sat is a by-product of the TiN bond. Therefore, the fraction of pyridinic-N can be extracted from the TiN fraction resulting in a critical contribution against the TiN fraction, as shown in Table 2. These results indicate that the transition from TiN to TiO_xN_y or $TiO_x(CN)_y$ is characterized by the TiN and pyridinic-N fraction.

Table 2 List of fitting parameters and fraction of chemical compositions for each element.

Name	Component	BE	FWHM	TiO_2	Brass	White gold	Rose gold	Bronze	Black
C-1	C-C/C-H	284.8-285.5	1.8-2.0	89.1	90.5	92.5	85.3	83.8	84.8
C-2	C-O	286.6-287.3	2.0	5.9	7.2	3.8	9.0	9.9	10.3
C-3	C=O	288.6-289.3	2.0	5.0	2.4	3.7	5.7	6.3	4.9
O-1	TiO_2	530.1	2.0	7.3	19.6	21.8	19.7	8.9	7.4
O-2	C-O/O=C-O	531.0	2.0	52.7	36.7	42.6	44.4	41.0	43.3
O-3	H_2O	532.8-533.0	2.0	39.9	43.6	35.6	35.9	50.1	49.3
N-1	TiO_xN_y	396.0	2.0	2.2	0.0	0.4	1.6	0.9	0.9
N-2	TiO_xN_y	396.4	2.0	2.2	26.3	1.6	25.9	12.7	0.1
N-3	TiN	397.8	2.0	10.4	45.5	65.9	15.2	7.5	0.1
N-4a	TiN-sat	399.5	2.0	3.7	5.9	10.8	5.6	3.5	0.0
N-4b	pyridinic N	399.5	2.0	31.8	7.0	5.6	31.0	42.9	59.4
N-5	pyrrolic N/N_2	401.0	2.0	49.8	15.2	15.7	20.8	32.6	39.6
T-1	TiN	456.0	2.2-3.0	4.3	18.6	13.8	10.5	13.7	10.5
T-2	TiO_xN_y	457.3	3.0	0.1	0.4	10.1	0.0	0.0	0.1
T-3a	TiN-sat	458.3	1.5-2.5	0.4	7.4	5.6	5.5	6.6	5.7
T-3b	TiO-III/Ti_xO_y	458.3	1.5-2.5	9.6	31.7	17.9	46.6	41.3	48.4
T-4	TiO-IV	459.5	1.4-1.8	85.7	41.9	52.6	37.3	38.3	35.3

The chemical compositions of Ti2p shown in Figure 5(h) are consistent with those of N1s in a way that TiN and TiO_xN_y fractions are high in Brass and White gold. As mentioned above, the TiO-III fraction can also be evaluated from the TiN-sat fraction that is proportional to the TiN fraction. As shown in Table 2, the TiO-IV fraction is high in Brass and White gold, and the TiO-III fraction is high in the other samples leading to the C and N contributions in the oxidation state. However, the fractions of TiN and TiO_xN_y are quantitatively different from those analyzed in N1s because the C and N contributions in the oxidation state complicate the quantitative chemical compositions based on Ti2p peak analysis.

Figure 6 shows NEXAFS spectra on TiO_2 and TiN-based films. TEY is less surface sensitive than XPS because the TEY signal is proportional to the secondary electron in the low kinetic energy range, which has a longer mean free path than the photoelectron and Auger electron [29]. TFY is not sensitive to the surface due to the transmission of light in films longer than that of electrons. Therefore, the TEY and TFY spectra reflect the subsurface and bulk electronic structures, respectively. TFY spectra are prone to deform when the elemental contents are high in the film because of the saturation and self-absorption effects [51-53].

TEY spectra of C *K* edges show a similar trend among the samples, as shown in Figure 6(a). The first peak at 284 eV represents the transition from 1s to Ti3d-C2p* states, and the broad edge at 291 eV corresponds to the transition from 1s to Ti4sp-C2p* states. The features between 285 and 290 eV originate from the pre-edge that consists of $\pi^*_{C\text{-}O\text{-}C,\ C\text{-}NH\text{-}C}$ at 287 eV, and $\pi^*_{C=O,\ C=C\text{-}NH2}$ and $\sigma^*_{C\text{-}H}$ at 288 eV [54,55]. The peak at 288 eV appears on all samples, while the peak at 287 eV is present on TiO_2, Brass, and White gold. TFY spectra of C *K* edges show a tail to low photon energy side and broadening below 290 eV in Black, Bronze, and Rose gold films as carbon content increases in films as observed in XPS, which suggests that the rock-salt TiC formation in TiN matrix [56].

O *K* edge of TiO_2 has a crystal field splitting between 530 and 533 eV leading to the t_{2g} and e_g peaks as shown in Figure 6(b) because of the transition from O1s to unoccupied states based on Ti3d-O2p π* and σ* states in the octahedral field, respectively [57]. The splitting is 2.7 eV in TiO_2, which agrees with the literature [58]. The peak splitting of TiN-based films is 2.3 eV evaluated on Black and Bronze. Brass, White, and Rose golds show a spectral difference at the first peak shape between TFY and TEY spectra resulting from the surface oxidation. The surface oxidation replaces the Ti-N bond with the Ti-O bond at the surface, modifying a multiplicity of molecular orbitals in a deformed octahedral field. Compared with TiO_2, the O *K* edges of TiN-based films are broad upon the increases in carbon and nitrogen species by a weakened and distorted octahedral field from the multiple bonds in the films in a way that C-O, C=O, O-N, and O=N. The spectral features above 537 eV represent the transition from O1s to O2p* mixed with Ti4sp* bands [59,60]. From the molecular orbit theory, their features correspond to Ti4s-O2p σ* (a_{1g}) and Ti4p-O2p π* (t_{1u}) in the TiO_2 spectrum, and their intensities indicate the rutile phase rather than the anatase phase [57,58,61].

N *K* edges in Figure 6(c) show that the first two peaks from the transition from N1s to N2p π* and σ* mixed with Ti3d*, resulting in the t_{2g} and e_g peaks from a crystal field splitting based on the molecular orbit theory of rock-salt TiN in the octahedral field. The crystal field splitting is about 2.7 eV in Brass, White, and Rose golds. The first two peaks are weakened upon both the decrease in nitrogen content and the increase in carbon content by a weakened and distorted octahedral field from multiple bonds in the films such as triple-bonded N_2, N-O, and N-C in the films [59,62-64]. In Black, and TEY of Bronze and Rose gold, the e_g peak is more intense than the t_{2g} peak because the unbound nitrogen peak appears close to the e_g peak position [23,60,65]. This suggests the unbound nitrogen increases in the subsurface of Black, Bronze, and Rose gold, which is consistent with the increase in N_2 observed in XPS N1s fitting results. N *K* edges have a slight difference between TFY and TEY spectra. The board features above 403 eV represent the transition from N1s to N2p* mixed with Ti4sp* bands resulting in the a_{1g} and t_{1u} from the molecular orbit theory of rock-salt TiN in the octahedral field. The central weights of these features shift lower energy from Brass to Black.

In Figure 6(d), Ti *L*3,2 edges of TEY in TiO_2 show the crystal field splitting of unoccupied Ti3d states as well as spin-orbit splitting of initial Ti2p states because the Ti *L*3,2 edge reflects the dipole transition from Ti2p to Ti3d* hybridized with O2p*. It is also found that, in TEY, the Ti *L*3 e_g peak, which is sensitive to the local environment due to the orbital orientation toward O2p, provides double peaks and asymmetry for the rutile phase of TiO_2 film at the

subsurface region [66], and which is consistent with the result of O *K* edge feature on TiO_2 film. However, the corresponding peak in TFY suggests double peaks in symmetry leading to an equivalent mixture between rutile and anatase TiO_2 in bulk. TFY spectra in Rose gold, Bronze, and Black have a serious self-absorption resulting in the saturation and deformation of spectra compared with the other TFY spectra. This result suggests that Ti contents are not high in Black and Bronze at surface of films as observed in Figure 4(b), while Ti contents might be high in bulk of films. Both TFY and TEY spectra present a leading-edge structure beside t_{2g} peak at *L*3 in Brass and White gold. However, it is difficult to distinguish the chemical bonding effect from the self-absorption effect in the spectra.

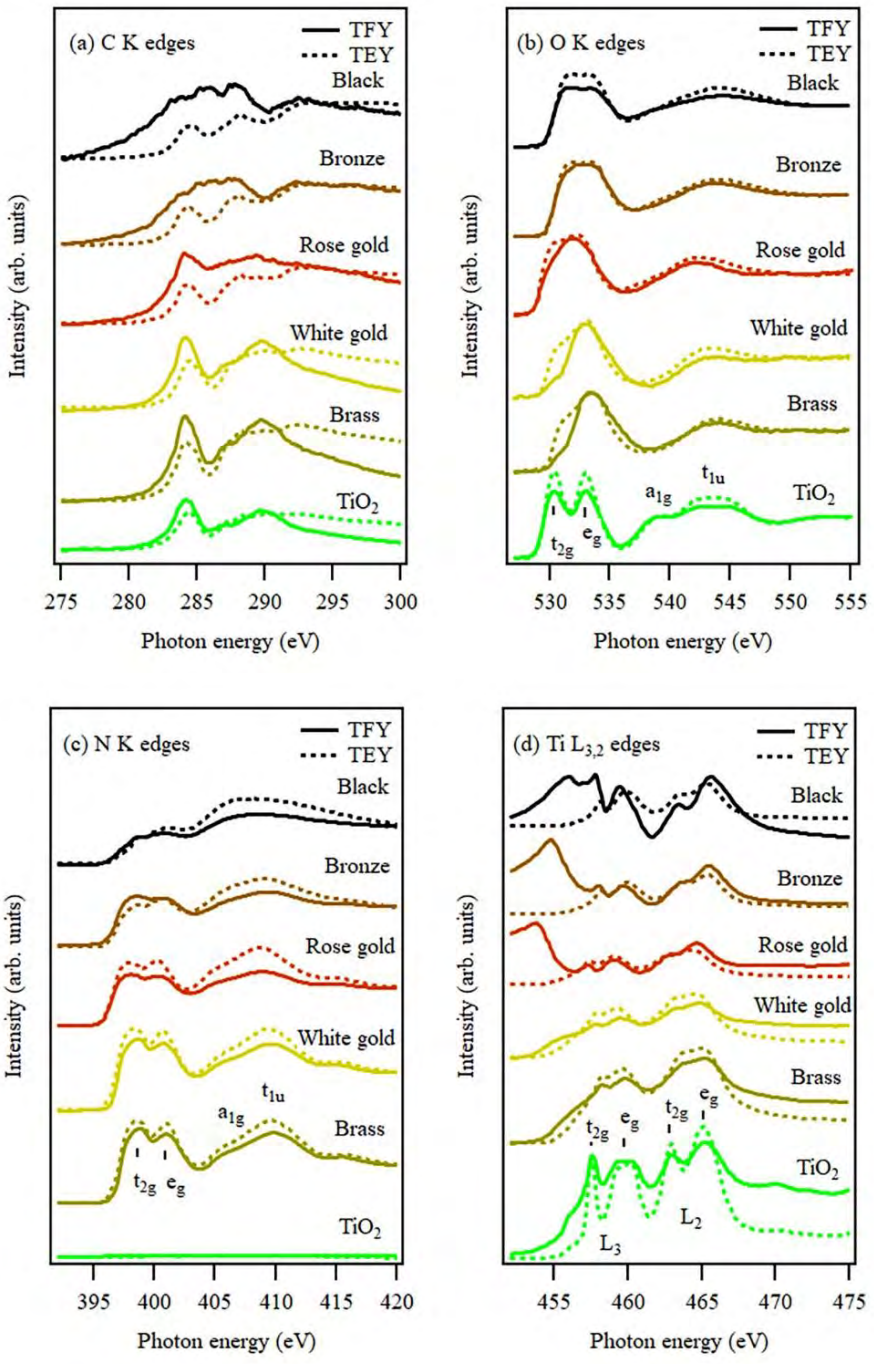

Figure 6 NEXAFS spectra measured on (a) C *K*, (b) O *K*, (c) N *K*, and (d) Ti *L*3,2 edges.

4. Conclusion

The electronic structures in Ti-based decorative films were measured at the surface, subsurface, and bulk regions by UPS, XPS, and NEXAFS techniques, respectively. The colors of Ti-based decorative films were measured in the CIELAB scheme. Surface contamination and oxidation effects were observed in the XPS and NEXAFS. The chemical compositions on the surface of Ti-based decorative film analyzed by XPS revealed that the films could be characterized by the Ti-N and pyridinic-N fractions in N1s spectra even under surface contamination and oxidation. NEXAFS spectra disclosed the chemical compositions in the subsurface and bulk of films. The signatures observed in NEXAFS were weaker than those in XPS because the NEXAFS spectra reflected the conjunct density of states of conduction bands. The crystal field splitting and unbound nitrogen peak were discerned in the N *K* edges. Soft X-ray spectroscopy provides a guide for the coloration of Ti-based decorative coatings and gives us a hint to improve functional electrodes in semiconductor devices. However, further studies on the morphology, crystallinity, and optical properties measured by X-ray diffraction, electron microscopy, Raman spectroscopy, and ellipsometry will be reported in the future.

.

Acknowledgment

Authors thank Thapanin Co., Ltd, NECTEC Opto-Electrochemical Sensing Research laboratory, and SLRI BL3.2Ua staff members for their technical support. HN thanks SLRI for internal research fund.

References

[1] P. Panjan, A. Drnovšek, P. Terek, A. Miletić, M. Čekada, M. Panjan, Comparative study of tribological behavior of TiN hard coatings deposited by various PVD deposition techniques, *Coatings* **12** (2022) 294.

[2] S. Jin, Y. Zhang, Q. Wang, D. Zhang, S. Zhang, Influence of TiN coating on the biocompatibility of medical NiTi alloy, *Colloids Surf. B* **101** (2013) 343-349.

[3] W-Y. Wu, M-Y. Chan, Y-H. Hsu, G-Z. Chen, S-C. Liao, C-H. Lee, P-W. Lui, Bioapplication of TiN thin films deposited using high power impulse magnetron sputtering, *Surf. Coat. Technol.* **362** (2019) 167-175.

[4] N. Ohtake, M. Hiratsuka, K. Kanda, H. Akasaka, M. Tsujioka, K. Hirakuri, A. Hirata, T. Ohana, H. Inaba, M. Kano, H. Saitoh, Properties and classification of diamond-like carbon films, *Materials* **14** (2021) 315.

[5] T. Huang, J. Guo, C. Kao, A comparison of the friction associated with diamond-like carbon (DLC) or titanium nitride (TiN) plating metal brackets, *Surf. Coat. Technol.* **205** (2010) 1917-1921.

[6] M. Łępicka, Y. Tsybrii, D. Kiejko, K. Golak, The effect of TiN and DLC anti-wear coatings on the tribofilm formation and frictional heat phenomena in coated metals vs. WC-Co, *Materials* **14** (2021) 3342.

[7] R. Constantin, P.-A. Steinmann, C. Anasterski, Decorative PVD coatings, In: J. Takadoum (Ed.), Nanomaterials and surface engineering, Chapter 5 (2013).

[8] E. L. Dalibón, J. N. Pecina, M. N. Moscatelli, M. A. R. Ramos, V. J. Trava-Airoldi, S. P. Brühl, Mechanical and corrosion behaviour of DLC and TiN coatings deposited on martensitic stainless steel, *J. Bio. Tribo. Corros.* **5** (2019) 34.

[9] X. L. Zhou, Y. P. Zheng, T. Shimizu, C. Euaruksakul, S. Tunmee, T. Wang, H. Saitoh, Y. B. Tang, Colorful diamond-like carbon films from different micro/nanostructures, *Adv. Optical Mater.* **8** (2020) 1902064.

[10] R. Constantin, B. Miremad, Performance of hard coatings, made by balanced and unbalanced magnetron sputtering, for decorative applications, *Surf. Coat. Technol.* **120–121** (1999) 728-733.

[11] S. Niyomsoan, W. Grant, D. L. Olson, B. Mishra, Variation of color in titanium and zirconium nitride decorative thin films, *Thin Solid Films* **415**, (2002) 187-194.

[12] L. Skowronski, M. Chorobinski, The effect of thickness and optical constants of the dielectric layer on the color behaviour of the glass/Ti/TiO_2 decorative coatings, *Thin Solid Films* **691** (2019) 137595.

[13] A. Yakovlev, V. Milichko, E. Pidko, V. V. Vinogradov, A. V. Vinogradov, Inkjet printing of TiO_2/AlOOH heterostructures for the formation of interference color images with high optical visibility, *Sci. Rep.* **6** (2016) 37090.

[14] E. O. Filatova, A. S. Konashuk, S. S. Sakhonenkov, A. U. Gaisin, N. M. Kolomiiets, V. V. Afanas'ev, H. F. W. Dekkers, Mechanisms of TiN effective workfunction tuning at interfaces with HfO_2 and SiO_2, *J. Phys. Chem. C* **124** (2020) 15547-15557.
[15] C. Zhao, J. Xiang, Atomic layer deposition (ALD) of metal gates for CMOS, *Appl. Sci.* **9** (2019) 2388.
[16] I. Z. Mitrovic, H. M. Przewlocki, K. Piskorski, G. Simutis, V. R. Dhanak, N. Sedghi, S. Hall, Effect of oxygen on tuning the TiN_x metal gate work function on $LaLuO_3$, *Thin Solid Films* **520** (2012) 6959-6962.
[17] Y. Lin, K. Huang, H. Lin, M. Chen, Effective work function modulation of the bilayer metal gate stacks by the Hf-doped thin TiN interlayer prepared by the *in-situ* atomic layer doping technique, *Solid State Commun.* **258** (2017) 49-53.
[18] J. Bi, R. Zhang, S. Peng, J. Sun, X. Wang, W. Chen, L. Wu, J. Gao, H. Cao, Y. Cao, Robust plasmonic properties of epitaxial TiN films on highly lattice-mismatched complex oxides, *Phys. Rev. Materials* **5** (2021) 075201.
[19] R. P. Sugavaneshwar, S. Ishii, T. D. Dao, A. Ohi, T. Nabatame, T. Nagao, Fabrication of highly metallic TiN films by pulsed laser deposition method for plasmonic applications, *ACS Photonics* **5** (2018) 814-819.
[20] R. Zhang, Q. Ma, H. Liu, T. Sun, J. Bi, Y. Song, S. Peng, L. Liang, J. Gao, H. Cao, L. Huang, Y. Cao, Crystal orientation-dependent oxidation of epitaxial TiN films with tunable plasmonics, *ACS Photonics* **8** (2021) 847–856.
[21] S. M. Borah, H. Bailung, J. Chutia, Decorative titanium nitride colored coatings on bell-metal by reactive cylindrical magnetron sputtering, *Prog. Color Color. Coat.* **3** (2010) 74-80.
[22] N. C. Saha, H. G. Tompkins, Titanium nitride oxidation chemistry: An x-ray photoelectron spectroscopy study, *J. Appl. Phys.* **72** (1992) 3072-3079.
[23] F. Esaka, K. Furuya, H. Shimada, M. Imamura, N. Matsubayashi, H. Sato, A. Nishijima, A. Kawana, H. Ichimura, T. Kikuchi, Comparison of surface oxidation of titanium nitride and chromium nitride films studied by X-ray absorption and photoelectron spectroscopy, *J. Vac. Sci. Technol. A* **15** (1997) 2521-2528.
[24] J. Schanda, Colorimetry: Understanding the CIE system, New York, US: John Wiley & Sons, Inc. (2007).
[25] H. Nakajima, S. Chaichuay, P. Sudmuang, S. Rattanasuporn, W. Jenpiyapong, R. Supruangnet, N. Chanlek, P. Songsiriritthigul, Commissioning of the soft X-ray undulator beamline at the Siam Photon Laboratory, *AIP Conf. Proc.* **1741** (2016) 020040.
[26] H. Nakajima, A. Tong-on, N. Sumano, K. Sittisard, S. Rattanasuporn, C. Euaruksakul, R. Supruangnet, N. Jearanaikoon, P. Photongkam, N. Chanlek P. Songsiriritthigul, Photoemission spectroscopy and photoemission electron microscopy beamline at the Siam Photon Laboratory, *J. Phys.: Conf. Ser.* **425** (2013) 132020.
[27] G. Greczynski, L. Hultman, Towards reliable X-ray photoelectron spectroscopy: Sputter-damage effects in transition metal borides, carbides, nitrides, and oxides, *Appl. Surf. Sci.* **542** (2021) 148599.
[28] G. Greczynski, L. Hultman, X-ray photoelectron spectroscopy: Towards reliable binding energy referencing, *Prog. Mater. Sci.* **107** (2020) 100591.
[29] H. Shinotsuka, S. Tanuma, C. J. Powell, D. R. Penn, Calculations of electron inelastic mean free paths. X. Data for 41 elemental solids over the 50 eV to 200 keV range with the relativistic full Penn algorithm, *Surf. Interface Anal.,* **47** (2015) 871-888.
[30] A. Jablonski, C. J. Powell, Effective attenuation lengths for different quantitative applications of X-ray photoelectron spectroscopy, *J. Phys. Chem. Ref. Data.* **49** (2020) 033102.
[31] G. Greczynski, L. Hultman, C 1s peak of adventitious carbon aligns to the vacuum level: Dire consequences for material's bonding assignment by photoelectron spectroscopy, *ChemPhysChem.* **18** (2017) 1507.
[32] G. Greczynski, L. Hultman, Reliable determination of chemical state in X-ray photoelectron spectroscopy based on sample-work-function referencing to adventitious carbon: Resolving the myth of apparent constant binding energy of the C 1s peak, *Appl. Surf. Sci.* **451** (2018) 99-103.
[33] G. Greczynski, L. Hultman, Compromising science by ignorant instrument calibration - Need to revisit half a century of published XPS data, *Angew. Chem. Int. Ed.* **59** (2020) 5002-5006.
[34] M. M. Nahid, E. Gann, L. Thomsen, Ch. R. McNeill, NEXAFS spectroscopy of conjugated polymers, *Eur. Polym. J.* **81** (2016) 532-554.

[35] E. Gann, C. R. McNeill, A. Tadich, B. C. C. Cowie, L. Thomsen, Quick AS NEXAFS Tool (QANT): A program for NEXAFS loading and analysis developed at the Australian Synchrotron, *J. Synchrotron Rad.* **23** (2016) 374-380.
[36] P. E. Batson, Carbon 1s near-edge-absorption fine structure in graphite, *Phys. Rev. B* **48** (1993) 2608.
[37] H. Nakajima (2021). hidecode221b/xps-excel-macro: EX3ms, https://doi.org/10.5281/zenodo.1320738.
[38] N. D. Lang, W. Kohn, Theory of metal surfaces: Work function, *Phys. Rev. B* **3** (1971) 1215.
[39] J. Y. Chia, T. Lertvanithphol, T. Chaikeeree, K. Seawsakul, N. Thamrongsiripak, H. Nakajima, P. Songsiriritthigul, M. Horprathum, N. Nuntawong, Work function alteration of the porous indium tin oxide nanorods film by electron beam irradiation technique, *Radiat. Phys. Chem.* **188** (2021) 109664.
[40] M. G. Helander, M. T. Greiner, Z. B. Wang, Z. H. Lu, Pitfalls in measuring work function using photoelectron spectroscopy, *Appl. Surf. Sci.* **256** (2010) 2602-2605.
[41] G. H. Major, N. Fairley, P. M. A. Sherwood, M. R. Linford, J. Terry, V. Fernandez, K. Artyushkova, Practical guide for curve fitting in X-ray photoelectron spectroscopy, *J. Vac. Sci. Technol. A* **38** (2020) 061203.
[42] J. H. Scofield, Hartree-Slater subshell photoionization cross-sections at 1254 and 1487 eV, *J. Electron Spectrosc. Relat. Phenom.* **8** (1976) 129-137.
[43] J. J. Yeh, I. Lindau, Atomic subshell photoionization cross sections and asymmetry parameters: $1 \leqslant Z \leqslant 103$, *At. Data Nucl. Data Tables* **32** (1985) 1-155.
[44] G. Greczynski, L. Hultman, Self-consistent modelling of X-ray photoelectron spectra from air-exposed polycrystalline TiN thin films, *Appl. Surf. Sci.* **387** (2016) 294-300.
[45] K. Haubner, J. Murawski, P. Olk, L. M. Eng, C. Ziegler, B. Adolphi, E. Jaehne, The route to functional graphene oxide. *ChemPhysChem.* **11** (2010) 2131-2139.
[46] J. Dupin, D. Gonbeau, P. Vinatier, A. Levasseur, Systematic XPS studies of metal oxides, hydroxides and peroxides, *Phys. Chem. Chem. Phys.* **2** (2000) 1319-1324.
[47] Y. Zhou, N. Wang, X. Qu, F. Huang, Y. Duan, X. Zhang, X. Dong, Z. Zhang, Arc-discharge synthesis of nitrogen-doped C embedded TiCN nanocubes with tunable dielectric/magnetic properties for electromagnetic absorbing applications, *Nanoscale* **11** (2019) 19994-20005.
[48] M. C. Biesinger, L. W. M. Lau, A. Gerson, R. St. C. Smart, Resolving surface chemical states in XPS analysis of first row transition metals, oxides and hydroxides: Sc, Ti, V, Cu and Zn, *Appl. Surf. Sci.* **257** (2010) 887-898.
[49] E. Faktorovich-Simon, A. Natan, E. Peled, D. Golodnitsky, Comparison of the catalytic activity of carbon, spinel-based, and carbide materials in the Na-Air battery, *Front. Mater.* **6** (2019) 249.
[50] D. Jaeger, J. Patscheider, A complete and self-consistent evaluation of XPS spectra of TiN, *J. Electron Spectrosc. Relat. Phenom.* **185** (2012) 523-534.
[51] S. Eisebitt, T. Böske, J.-E. Rubensson, W. Eberhardt, Determination of absorption coefficients for concentrated samples by fluorescence detection, *Phys. Rev. B* **47** (1993) 14103.
[52] D. Asakura, E. Hosono, Y. Nanba, H. Zhou, J. Okabayashi, C. Ban, P. Glans, J. Guo, T. Mizokawa, G. Chen, A. J. Achkar, D. G. Hawthron, T. Z. Regier, H. Wadati, Material/element-dependent fluorescence-yield modes on soft X-ray absorption spectroscopy of cathode materials for Li-ion batteries, *AIP Adv.* **6** (2016) 035105.
[53] F. Frati, M. O. J. Y. Hunault, F. M. F. de Groot, Oxygen K-edge X-ray absorption spectra, *Chem. Rev.* **120** (2020) 4056-4110.
[54] K. G. Latham, M. I. Simone, W. M. Dose, J. A. Allen, S. W. Donne, Synchrotron based NEXAFS study on nitrogen doped hydrothermal carbon: Insights into surface functionalities and formation mechanisms, *Carbon* **114** (2017) 566-578.
[55] Y. Zhao, Z. Wang, G. J. Xu, M. D. Li, Impact of EGR on the surface functional groups of diesel engine particles based on NEXAFS, *RSC Adv.* **6** (2016) 57363-57370.
[56] J. G. Chen, J. Eng Jr., S. P. Kelty, NEXAFS determination of electronic and catalytic properties of transition metal carbides and nitrides: From single crystal surfaces to powder catalysts, *Catal. Today* **43** (1998) 147-158.

[57] L. A. Grunes, R. D. Leapman, C. N. Wilker, R. Hoffmann, A. B. Kunz, Oxygen K near-edge fine structure: An electron-energy-loss investigation with comparisons to new theory for selected 3d Transition-metal oxides, *Phys. Rev. B* **25** (1982) 7157.

[58] R. Brydson, H. Sauer, W. Engel, F. Hofer, Electron energy-loss near-edge structures at the oxygen K edges of titanium(IV) oxygen compounds, *J. Phys.: Condens. Matter* **4** (1992) 3429.

[59] F. M. F. de Groot, J. C. Fuggle, B. T. Thole, G. A. Sawatzky, $L_{2,3}$ X-ray-absorption edges of d_0 compounds: K^+, Ca^{2+}, Sc^{3+}, and Ti^{4+} in Oh (octahedral) symmetry, *Phys. Rev. B* **41** (1990) 928.

[60] E. O. Filatova, A. S. Konashuk, S. S. Sakhonenkov, A. A. Sokolov, V. V. Afanas'ev, Re-distribution of oxygen at the interface between γ -Al_2O_3 and TiN, *Sci. Rep.* **7** (2017) 4541.

[61] C. Mitterbauer, G. Kothleitner, W. Grogger, H. Zandbergen, B. Freitag, P. Tiemeijer, F. Hofer, Electron energy-loss near-edge structures of 3d transition metal oxides recorded at high-energy resolution, *Ultramicroscopy* **96** (2003) 469-480.

[62] B. J. Murdoch, R. Ganesan, D. R. McKenzie, M. M. M. Bilek, D. G. McCulloch, J. G. Partridge, Influence of nitrogen-related defects on optical and electrical behaviour in $HfO_{2-x}N_x$ deposited by high-power impulse magnetron sputtering, *Appl. Phys. Lett.* **107** (2015) 112903.

[63] S. Campisi, C. E. Chan-Thaw, A. Villa, Understanding heteroatom-mediated metal–support interactions in functionalized carbons: A perspective review, *Appl. Sci.* **8** (2018) 1159.

[64] R. J. S. Skinner, J. S. Lee, Y.-F. Hu, D.-T. Jiang, P. Aich, S. Wettig, J. Maley, R. Sammynaiken, Local structure of M-DNA at the nitrogen K-edge: Evidence towards a metal ion induced conduction band in DNA, *J. Nanosci. Nanotechnol.* **5** (2005) 1557-1560.

[65] S. C. Chen, K. Y. Sung, W. Y. Tzeng, K. H. Wu, J. Y. Juang, T. M. Uen, C. W. Luo, J-Y. Lin, T. Kobayashi, H. C. Kuo, Microstructure and magnetic properties of oxidized titanium nitride thin films in situ grown by pulsed laser deposition, *J. Phys. D: Appl. Phys.* **46** (2013) 075002.

[66] R. Brydson, H. Sauer, W. Engel, J. M. Thomass, E. Zeitler, N. Kosugi, H. Kuroda, Electron energy loss and X-ray absorption spectroscopy of rutile and anatase: A test of structural sensitivity, *J. Phys.: Condens. Matter* **1** (1989) 797.